New Spatiotemporal Approaches for Fully Refocused, Multislice Ultrafast 2D MRI

Rita Schmidt and Lucio Frydman*

Purpose: Single-scan multislice acquisition schemes play key roles in magnetic resonance imaging. Central among these "ultrafast" experiments stands echo-planar imaging, a technique that although of optimal sampling is challenged by T_2* artifacts. Recent studies described alternatives based on spatiotemporal encoding (SPEN), which are particularly robust if implemented in a "full-refocusing" mode. This work extends this modality from the single-slice acquisitions in which it has hitherto been implemented, by introducing a variety of multislice schemes scanning 3D volumes.

Methods: Multislice SPEN employing either inversion or stimulated echo pulses and timed to fulfill the demands of full refocusing, are demonstrated. The performance of the ensuing methods was examined in "Hybrid" modalities encoding data in k- and direct-space, in low-specific absorption rate stimulated-echo approaches, and in direct-space SPEN approaches.

Results: When applied in phantoms and in in vivo systems, the ensuing single-shot sequences evidenced similar robustness, sensitivity, and resolution qualities as previously discussed 2D single-slice schemes, while enabling a rapid sampling of the third dimension via multislicing.

Conclusion: The unique benefits deriving from fully refocused, multislice, single-scan SPEN sequences were corroborated by phantom tests, as well as by in vivo scans at 3 and 7 T. Low specific absorption rate multislice SPEN variants compatible with human studies were demonstrated. **Magn Reson Med 71:711-722, 2014. © 2013 Wiley Periodicals, Inc.**

Key words: spatiotemporal encoding; single-shot MRI; super-resolution; full refocusing; multislice acquisitions; 3D imaging

Ultrafast magnetic resonance imaging (MRI) methods capable of completing a full multidimensional scan in subsecond timescales (1–6), affect a growing gamut of modern research and clinical MRI applications. These include, among others, diffusion, functional, flow, thermometric, and real-time three-dimensional studies (7–10). Mansfield's echo planar imaging [EPI, (1)] lies at the core of many such applications, usually in a format that scans multiple 2D slices in a train of consecutive acquisitions. This multislice format results in a fast and sensitive way of scanning a 3D volume, which is especially relevant in diffusion and functional MRI. Multislice EPI may, however, be vulnerable to magnetic field inhomogeneities and to frequencies offset effects; as well as potentially limited by the folding of objects placed beyond the targeted field-of-view [FOV (6,11,12). These weaknesses become particularly significant when considering their action along EPI's low-bandwidth, phase-encoded direction (11,13,14). An alternative approach explored in recent years and capable of alleviating these factors, is based on the image's spatiotemporal encoding (SPEN). This approach employs a chirped excitation of the spins under the action of a field gradient, of the kind proposed by Pipe and Kunz in the 1990's (15,16). Chirped excitations under the action of field gradients find important applications in the acquisition of arbitrary 2D nuclear magnetic resonance (NMR) data sets within a single scan (17,18), a feature that in recent years has renewed interest in their use for ultrafast 2D MRI acquisitions (19,20). In particular, numerous advantages have been demonstrated for "Hybrid" single-shot schemes relying on conventional k-space encoding along the high-bandwidth (readout) direction, and on SPEN to scan the image along the more artifact-prone, low-bandwidth axis (19–22). Two of the main drawbacks handicapping these methods vis-à-vis EPI, relating to a relatively lower image resolution and higher specific absorption rates (SARs), were alleviated by the introduction of super-resolution (SR) reconstruction methods along the SPEN acquisition dimension (23). While still based on principles differing from Fourier-Transform (FT) NMR/MRI, SR endowed SPEN with EPI-like resolutions, while allowing one to decrease the bandwidth of the chirp pulse, and with it the SAR of the scan. Another attractive feature of the resulting method relates to its high immunity to B_0 inhomogeneities and offsets, particularly if executed under "full-refocusing" conditions whereby each spin packet fully refocuses its T_2*/shift effects at the instant corresponding to its signal emission (21,24). Diffusion, fMRI and spectroscopic imaging experiments performed with this technique, show increasingly promising results (25–28).

A challenge still facing SPEN experiments, particularly those operating under full-refocusing conditions, concerns their implementation in fast volumetric imaging. Indeed, single-slice versions of these experiments could be robustly achieved by following the initial 90° encoding chirp pulse with a slice-selective 180° pulse (24); volumetric imaging extensions of these experiments have been implemented by phase encoding the third dimension (29)–but neither of these schemes enables

Department of Chemical Physics, Weizmann Institute of Science, Rehovot, Israel.

Grant sponsor: Kamin-Yeda Project (Israel Ministry of Trade and Industry); Grant number: 711237; Grant sponsor: ERC Advanced; Grant number: 246754; Grant sponsor: DIP Collaborative Project (Federal German Ministry for Education and Research); Grant number: 710907; Grant sponsor: Helen and Martin Kimmel Award for Innovative Investigation; Grant sponsor: Perlman Family Foundation.

*Correspondence to: Lucio Frydman, Department of Chemical Physics, Weizmann Institute of Science, Rehovot, Israel. E-mail: lucio.frydman@weizmann.ac.il

Received 7 October 2012; revised 4 February 2013; accepted 5 February 2013

DOI 10.1002/mrm.24714
Published online 6 March 2013 in Wiley Online Library (wileyonlinelibrary.com).

rapid multislice operation. A multislice SPEN imaging option was actually demonstrated using a selective excitation followed by a prescan 180° chirp pulse for imparting the spatial encoding, and a post-scan 180° chirp pulse "rewinding" all the nonexcited magnetization back into the longitudinal *z* axis (29). This version, however, cannot accommodate the full-refocusing mode alluded to earlier. This work comes to address this issue by exploring the performance of a variety of new SPEN-based schemes, incorporating slice-selective excitations as well as full-refocusing abilities, and in certain cases endowed with reduced SARs despite their rapid pulsing. Four of the new proposals employ the aforementioned "Hybrid" k/SPEN approach to scan in a single shot, 2D images in a multislice-compatible fashion; a fifth version is also proposed that implements the slices' 2D imaging on the basis of a pure SPEN approach encoding a two-dimensional plane. The parameters needed to implement these various sequences under full-refocusing conditions are described, and tests on phantoms assessing basic image quality, sensitivity, contrast and SAR properties, are presented. Features making each of these new options more or less favorable in particular cases are discussed, and the sequences' advantages are demonstrated in animal and human experiments collected at 3 and 7 T.

METHODS

Background: Principles of "Hybrid" SPEN/k-space Multislice MRI

As described in (29), multislice operation can benefit from imparting the quadratic phase being sought in SPEN by a 180° chirp pulse, rather than by the usual 90° chirp. The ensuing pulse will act as a progressive spin-echoing for a slice that has been targeted, and as a longitudinal inversion for all remaining spins in the sample. Disregarding chemical shift or other offset effects and assuming a radio frequency (RF) sweep inverting linearly and symmetrically the targeted FOV along the *y*-axis, this pulse will imprint a parabolic phase profile on the excited slice according to

$$\varphi_{180}(y) = -\frac{\gamma G_{180} T_{180}}{FOV_y} y^2 - \frac{\gamma G_{180} T_{180} \mathrm{FOV}_y}{4} \qquad [1]$$

where G_{180} and T_{180} are the gradient strength and the pulse duration during the 180° sweep. The constant-phase term in Eq. [1] is immaterial, whereas the quadratic term imposes a "focus" that defines the dominant region contributing at any given time to the observable free induction decay (FID). SPEN exploits this focus to investigate an object's density: if the minimum of the symmetric parabola in Eq. [1] is shifted by an initial purging gradient of area $|k_{\mathrm{prg}}| = \gamma G_{180} T_{180}$ toward an edge of the FOV to be scanned, and the ensuing FID is monitored as a function of an acquisition time *t* while under the action of a suitable gradient G_{acq}, the sample's density *ρ(y)* will be probed in a point-wise manner as different positions fulfill the stationary-phase condition (19)

$$\frac{\partial}{\partial y}\left[\varphi_{180}(y) + \left(k_{\mathrm{prg}} + \gamma G_{\mathrm{acq}} t\right) y\right]_{y=y_{\mathrm{SPC}}} = 0 \qquad [2]$$

An image thus becomes available; not by FT but rather by direct analysis of the FID's magnitude, as the stationary phase condition in Eq. [2] displaces along the *y*-axis according to $y_{\mathrm{SPC}} = -(\mathrm{FOV}_y/2) + \mathrm{FOV}_y(t/T_{\mathrm{acq}})$. It follows that to rasterize in this fashion the full FOV_y targeted by the 180° chirp, the acquisition gradient G_{acq} needs to be applied over a time T_{acq} fulfilling the condition $2 \cdot G_{180} T_{180} = \int_0^{T_{\mathrm{acq}}} G_{\mathrm{acq}}(t)\, dt$.

A number of complications will be associated with this imaging mode. One relates to the relatively strong gradients that SPEN will need to achieve resolutions comparable to those afforded by usual k-space acquisitions. This can be solved by replacing the simple magnitude-mode |FID(*t*)| reconstruction of the spins' image by a SR algorithm (23) involving inverting the equation $\mathrm{FID}(t) = A(y,t)\rho(y)$, where *A* is an a priori known matrix involving the pulse's details. This can be done non-iteratively based on the relation $\rho(y) = A^{\dagger}_{\mathrm{weighted}}(y,t) FID(t)$, where $A^{\dagger}$ is *A*(*y*,*t*)'s complex conjugate matrix, that can be found after suitable weighting the later about its central diagonal to better stabilize the inversion process (23). A second complication to be solved relates to the fact that 180° RF sweep will not only encode the slice that was selected, but also invert the spins' states in all remaining slices. To deal with the bulk spin saturation that this eventually will lead to, Ref. 29) proposed to restore all nonencoded spins back to their thermal equilibrium ($+M_z$) states by incorporating suitable broadband inversion pulses immediately after completing a single-slice 2D MRI acquisition. The position of this second inversion pulse can in fact be manipulated; in this study, we changed its placement to fulfill the demands imposed by full-refocusing.

Multislice SPEN Under Fully Refocusing

The purpose of this work is to introduce and compare the performance of multislice SPEN variants, capable of delivering their images under full-refocusing conditions. Full-refocusing is a special kind of echo aiming to remove all field and shift heterogeneities. This demands that the time elapsed since a particular *y*-dependent spin-packet is excited until the time it is inverted by 180° echoing pulse, be equal to the subsequent delay elapsed until its stationary-phase condition is fulfilled, and hence its signal becomes observable. The acquired signals will then be freed from any field inhomogeneities and/or offset effects experienced by a spin-packet, leading to images that are largely immune to T_2* and/or offset distortions. This can become a substantial advantage if the usually vulnerable low-bandwidth dimension of an EPI scan is replaced by this kind of SPEN strategy, whereas a traditional k-encoding is used to image the remaining read-out (*x*) axis. SPEN sequences involving a 90° chirp RF pulse can achieve full

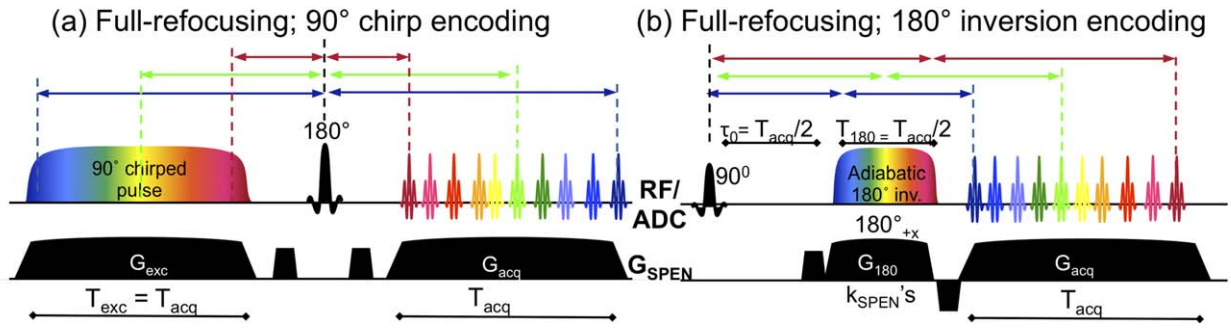

FIG. 1. Schematic description of SPEN's full-refocusing principles, illustrated for (**a**) a 90° chirp RF in charge of doing the encoding (24), and (**b**) a 180° adiabatic sweep variant introduced in this study. In both cases, the formation of echoes throughout the acquisition process is illustrated with arrows for three specific spin packets (indicated by blue, green, and red colors), whose frequencies are made inequivalent by the SPEN gradient (G_{SPEN} line). The RF/ADC line displays both the pulses and the timing of the acquisitions (ADC for Analogue-to-Digital Converter). Notice that in all cases, the times elapsed between the spin packets' excitation and inversion, equal the times elapsed between their simultaneous (a) or sequential (b) inversions and the time at which they elicit their corresponding signals according to the stationary phase condition (colored arrows). [Color figure can be viewed in the online issue, which is available at wileyonlinelibrary.com.]

refocusing simply by inserting a hard 180° pulse between excitation and acquisition processes set to fulfill the $T_{90}^{exc} = T_{acq}$ condition (Fig. 1a): the duration elapsed between every spin's excitation and its refocusing, will then be equal to that elapsed between its refocusing and the subsequent fulfillment of Eq. [2]. SPEN encoding by an inversion pulse breaks this symmetry, since during the course of this chirp spin-packets will refocus at different times $t_{180}^{inv}(y) = \left(\frac{y}{FOV_y} + \frac{1}{2}\right)$, depending on their position $-FOV_y/2 \leq y \leq +FOV_y/2$. When coupled to the y_{spc} conditions raised by Eq. [2], it follows that the net phase imparted by a field inhomogeneity $\Delta B_o(\vec{r})$ (or by a chemical shift) over the course of the SPEN excitation/evolution/inversion-encoding/gradient-decoding process, will be

$$\Delta\phi(\vec{r}) = \begin{cases} \gamma\Delta B_o(\vec{r})\left[T_{180} - 2\left(t_{180}^{inv}(y) - \tau_o\right)\right] = -\gamma\Delta B_o(\vec{r})\left[\frac{2T_{180}}{FOV_y}y + \tau_o\right], & \textit{during the encoding process} \\ \gamma\Delta B_o(\vec{r})t = \gamma\Delta B_o(\vec{r})\left[\frac{T_{180}G_{180}}{G_{acq}^{-}}\left(\frac{2y}{FOV_y} + 1\right)\right], & \textit{during the decoding process} \end{cases} \quad [3]$$

Here τ_o is an ancillary delay that will enable the achievement of the full-refocusing conditions, and for simplicity, we assumed that G_{acq}^{-} represents an average acquisition gradient strength. Given the aforementioned $2 \cdot G_{180}T_{180} = \int_0^{T_{acq}} G_{acq}(t)dt = T_{acq}G_{acq}^{-}$ condition, Eq. [3] predicts that the overall effects of $\Delta B_o(\vec{r})$ will vanish if $T_{acq} = 2T_{180}$; $\tau_o = T_{180}$. These events are pictorially illustrated for this 180° swept RF case in Figure 1b.

When considering the extension of these arguments to multislice SPEN/k-encoded 2D single-shot frameworks, the new scheme shown in Figure 2a results. Transforming the resulting data into a 2D image requires 1D FT along the readout axis, and SR processing along the SPEN dimension. Notice that this sequence concludes with a postacquisition hard 180° pulse, restoring all spins that were not targeted by the initial slice-selective excitation, back to a thermodynamically stable $+M_z$ state that is suitable for subsequent slice-selective acquisitions. Still, this restoration only takes effect after all spins have remained throughout the acquisition time (plus eventual spoiler delays) out of equilibrium. Figure 2b reduces this delay by modifying the scheme just described, and placing the restoring hard 180° pulse before the acquisition process. An analysis analogous to the one leading to Eq. [3] shows that full-refocusing conditions can also be reached in this case, provided that the positions of the 180° RF sweep and of the τ_o free-evolution delay are swapped, all other timing and gradient-strength conditions remaining unchanged.

A drawback that can limit the applicability of the two approaches just described, relates to the relatively high SAR that these sequences may display vis-à-vis multislice EPI. Indeed swept 180° RF pulses have higher SAR than both chirped and selective 90° pulses, and while these differences may not be limiting in single-slice studies endowed with relatively long repetition times (TRs), SAR may become a rate determining factor under fast-repetition multislice operation. To deal with this eventuality, Figure 2c introduces a different fully refocused Hybrid SPEN version, which reduces SAR by rearranging (at least conceptually) the various elements partaking of the sequence in Figure 2b. Foremost among these rearrangements is the interchange of the slice-selective and of the SPEN-encoding pulse positions. With this provision only a single 180° swept pulse is involved per volumetric scan, and the SAR per unit time becomes reduced by a factor approaching the number of slices involved. To preserve the ensuing quadratic spatial encoding for all encoded

slices, also the nature of the hard 180° restoring pulse is changed: it is split into two 90° pulses, one performing an initial bulk excitation and the other a postencoding storage. Effectively, this leads to a stimulated-echo variant of the spin-echo sequence introduced in Figure 2b. An obvious penalty of the resulting approach will be a signal loss, factoring in both a factor of ½ due to the intermediate storage stage, and additional losses stemming from T_1 relaxation effects that progressively recalled slices undergo. Given the significant SAR-reducing promises arising from this permutation, we also consider here the incremented excitation variant in Figure 2d. This version replaces the hard-90°/swept-180° encoding combination in Figure 2c by a chirp-90° encoding, and modifies the gradient and timing values accordingly to ensure the preservation of the desirable full-refocusing conditions. A distinction worth noting between this sequence based on a 90°-chirp encoding and its 180° swept pulse counterparts, rests in the fact that its effective echoing times lie in the $0 \leq \text{Echo Time (TE)} \leq 2T_{acq}$ regime rather than in the $T_{acq} \leq \text{TE} \leq 2T_{acq}$ interval.

Fully Refocused Multislice 2D MRI Acquisitions Based on Biaxial SPEN Encoding

In addition to these Hybrid SPEN/k-space scanning modes, multislice sequences are also well suited to fully spatiotemporally encoded single-scan acquisitions. Single-scan acquisitions involving SPEN MRI as the sole 2D encoding mode, were investigated in (30) with in vitro tests using consecutive 180° chirp pulses acting under orthogonal gradients. This biaxial SPEN option (bi-SPEN), preceded by suitable slice-selective excitations, is here adapted for in vivo studies as shown in Figure 3. This sequence involves a pair of pulses imparting a 2D elliptic paraboloid, whose minimum $r_{spc} = (x_{spc}, y_{spc})$ fulfills a stationary phase condition akin to that in Eq. [2],

$$\nabla_r \left[\varphi_{180}(\vec{r}) + \vec{k_{prg}} \cdot \vec{r} + \gamma \vec{k_{acq}} \cdot \vec{r} \right] = \vec{0} \qquad [4]$$

$$\left(\frac{\partial}{\partial y} \left[\frac{G^y_{180} T^y_{180}}{\text{FOV}_y} y^2 + k^y_{prg} y + \gamma \int G^y_{acq}(t) dt y \right], \frac{\partial}{\partial x} \left[-\frac{G^x_{180} T^x_{180}}{\text{FOV}_x} x^2 + k^x_{prg} x + \gamma \int G^x_{acq}(t) dt x \right] \right)_{\vec{r}=\vec{r}_{spc}} = (0,0)$$

where constant phase terms have been disregarded. This paraboloid's stationary-phase can be moved around over the course of the acquisition via suitably tailored gradients $G^x_{acq}(t)$, $G^y_{acq}(t)$, rasterizing in such fashion the 2D imaging information being sought directly in the spatial domain, with no need for FT along any dimension (Fig. 3b). A challenge posed by such strategy then arises if seeking to fulfill full-refocusing conditions. One possible solution consists of adopting the scheme given in Figure 2b, with the hard pulse replaced by a 180° chirp encoding pulse acting along what would become the "fast" SPEN direction. This imposes a significant symmetry break in the tasks, time-scales, and performances ascribed to the two orthogonal SPEN pulses: an initial, longer RF pulse becomes charged with encoding a slowly rasterized dimension and a second pulse is in charge of encoding a rapidly scanned axis. Referring to these two directions as the "slow" and "fast" axes of the bi-SPEN acquisition respectively (Fig. 3a), it follows that scanning the relevant FOV's will still demand fulfilling conditions similar to those given above: $2 \cdot G^{fast}_{180} T^{fast}_{180} = \int_0^{T^{fast}_{acq}} G^{fast}_{acq}(t) dt$ along the rapidly readout axis, and $2 \cdot G^{slow}_{180} T^{slow}_{180} = \int_0^{T^{slow}_{acq}} G^{slow}_{acq}(t) dt$ along the slowly blipped axis. Given the orders-of-magnitude that separate the $T^{slow}_{180}, T^{fast}_{180}$ encoding times, and thereby the $T^{slow}_{acq}, T^{fast}_{acq}$ used to rasterize the slow and fast dimensions in this simple Cartesian scheme, the conditions required for refocusing inhomogeneities in the ensuing 2D bi-SPEN sequence become very similar to those derived earlier for the Hybrid sequence in Figure 2b. In this mode, full refocusing is achieved for every other rapidly scanned line if an interchirp-pulse delay τ_o is introduced fulfilling $\tau_o = T^{slow}_{180} = T^{slow}_{acq}/2$ and if $T^{fast}_{180} = T^{fast}_{acq}/2 << T^{slow}_{180}$.

One complication associated with such scheme arises from the short encoding periods that this form of full-refocusing will demand from the "fast" dimension. Even if relying on high performance systems, practical parameters in an animal scanner would be limited to $T^{fast}_{180} = 0.3$ ms, $G^{fast}_{180} = 40$ G/cm; for a FOV = 3 cm this predicts a spatial resolution $\Delta r = \sqrt{\frac{\text{FOV}}{2\gamma G_{180} T_{180}}} = 2\text{–}3$ mm (11) –much larger than the <0.5 mm values normally being sought. A similarly large difference would arise if assuming high performance values for a clinical setting, reaching ca. 15 mm resolutions for a 30 cm FOV rather than the 1–2 mm normally sought. Super Resolution thus becomes a critical component for bypassing this limitation of fully refocused bi-SPEN 2D MRI. In fact, implementing the SR algorithm in these cases in principle will involve solving a different problem than the $\rho(y) = A^{\dagger}_{weighted}(y,t)\text{FID}(t)$ counterpart mentioned earlier. That was a 1D problem, whose solution was repeated in a row-by-row fashion for all values of k_x/x; for 2D bi-SPEN the SR reconstruction is a higher dimensional problem, requiring the solution of $\text{FID}(t) = A(x,y,t) \cdot \rho(x,y)$ for a particular acquisition pattern arrangement. This expression can be rearranged as $\rho(\vec{r}) = A^{\dagger}(t,\vec{r})\text{FID}(t)$, where the $A^{\dagger}$ matrix is of size N_tx($N_x \cdot N_y$) with N_x and N_y the number of acquired points in the fast and slow dimensions, and N_t the total number of digitized FID points. For a Cartesian acquisition like the one in Figure 3a this $A^{\dagger}$ matrix will have $\approx (N_x \cdot N_y)^2$ elements, making the reconstruction of the spin density a memory and computational onerous problem, even for a modest 64 × 64 final 2D imaging matrix. To solve this challenge, a customized code was written that performs the SR reconstruction after dividing the overall matrix onto smaller parts and executing the inversions and multiplications of the

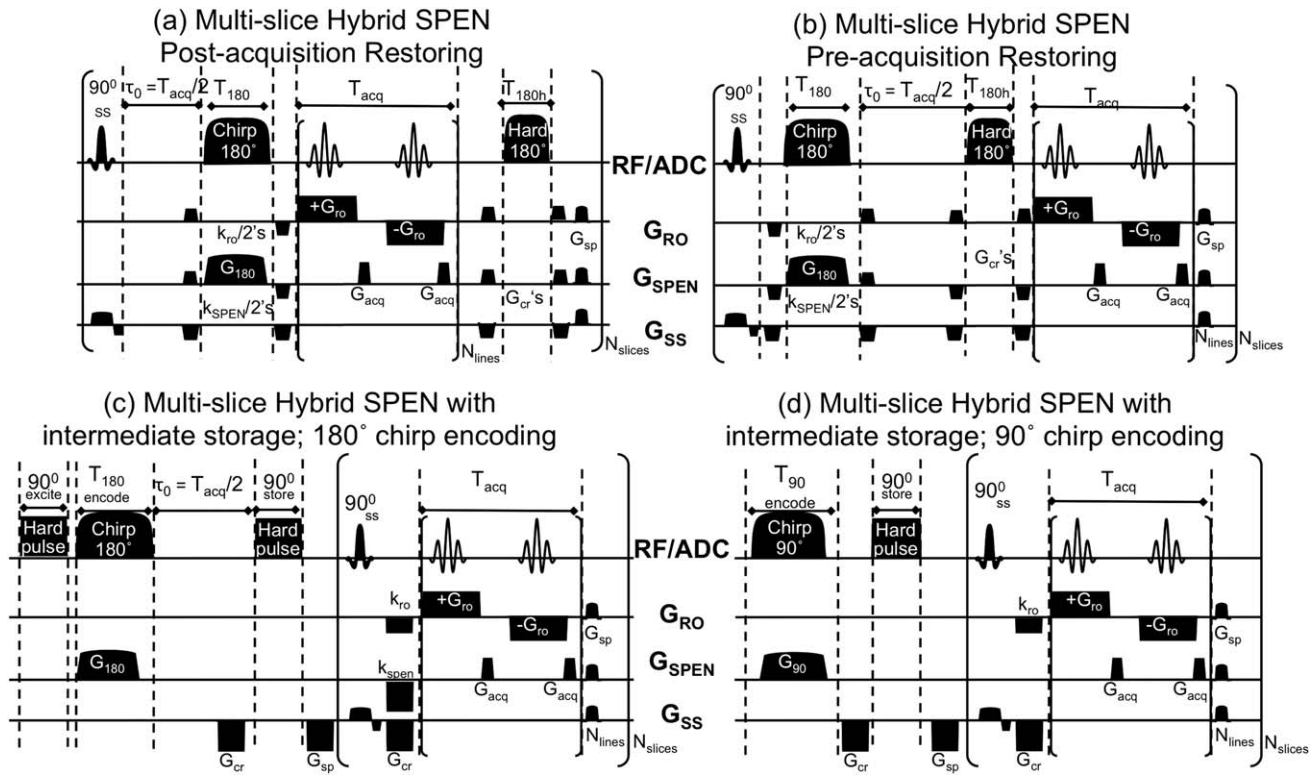

FIG. 2. Multislice single-shot Hybrid SPEN/k-space sequences fulfilling full-refocusing conditions. **a** and **b**: Operate on the basis of 180° chirp encoding and 180° hard rewinding pulses: in the first option the latter is applied after the acquisition, while in the second it is applied before it. **c** and **d**: They are Hybrid alternatives replacing the hard 180° pulse with stimulated echoes, and doing the spatial encoding with 180° and with 90° chirp pulses, respectively. G_{RO}, G_{SPEN}, and G_{SS} denote the gradients applied along the readout, the spatiotemporally encoded, and the slice-selective directions, respectively. Main parameters of the scans: T_{acq}, G_{acq}, acquisition duration and gradient strength associated to the low-bandwidth SPEN dimensions; T_{ro}, G_{ro}, acquisition duration and gradient strength associated with the orthogonal k-space readout dimension; N_{slices}, N_{lines}, number of slice-selective and of SPEN-decoded elements; T_{180}, G_{180}, chirp pulse duration and associated gradient strength; k_{ro} and k_{SPEN}, pairs of prewinding gradients flanking the adiabatic 180° inversion and imparting $\approx \Upsilon G_{ro} T_{ro}/2$ and $\approx \Upsilon G_{180} T_{180}$ encodings, respectively; G_{cr} and G_{sp}, crusher and spoiler gradients applied on all axes.

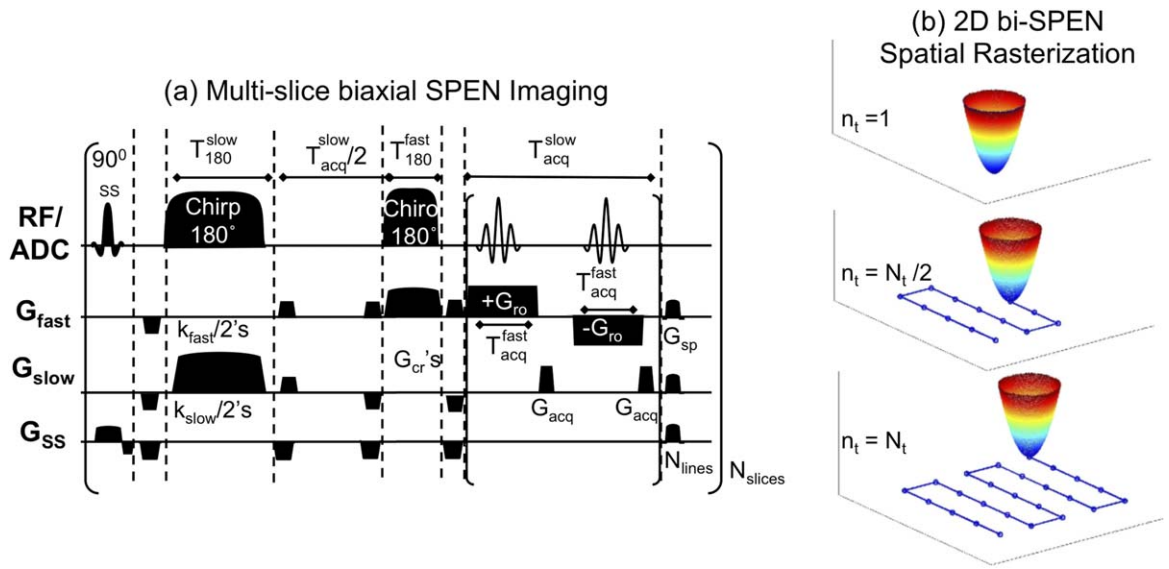

FIG. 3. **a:** Multislice single-shot 2D bi-SPEN sequence fulfilling full-refocusing conditions. G^{fast} and G^{slow} represent gradients encoding two orthogonal directions; T^{fast}_{acq}, G^{fast}_{acq}, T^{slow}_{180}, G^{slow}_{180}, T^{fast}_{180}, G^{fast}_{180} are the duration/gradient strengths associated with the acquisitions and encodings of the respective dimensions; k_{fast} and k_{slow} are prewinding gradients of actions $\Upsilon G^{fast}_{180} T^{fast}_{180}$, $\Upsilon G^{slow}_{180} T^{slow}_{180}$; all remaining symbols are as in Figure 2. The number of acquired points in the "slow" direction is $N_y = 2 \cdot N_{lines}$, and in the "fast" one $N_x = T^{fast}_{acq} \cdot SW$ **b**: Schematic representation of the trajectory experienced by 2D paraboloid generated in the encoding (a), for three points (beginning, halfway, and conclusion) of the data acquisition process. [Color figure can be viewed in the online issue, which is available at wileyonlinelibrary.com.]

relevant components using regions that are smaller than the full FOV In addition to this bi-axial reconstruction method, the use of the 1D SR algorithm described earlier was also assayed, acting first along one and subsequently along the other SPEN dimension. Driving these tests was the very different time-scales associated with the encoding along the "slow" and "fast" axes, and suggesting that sufficient resolution is endowed by the prolonged T_{180}^{slow} anyhow to make the improvements of the SR procedure along this axis relevant.

Experimental

Experiments assaying the relative resolution, sensitivity and robustness of the various sequences introduced in Figures 2 and 3, were first collected on phantoms using a 7T Varian VNMRS vertical imaging 89 mm bore system and a horizontal 3T Siemens TIM TRIO clinical platform. The spin-echo EPI single-scan acquisitions proved particularly challenging for the vertical 7T hardware and artifacts remained even after data sets were processed using customized echo alignment and shearing procedures. EPI experiments were more robust at 3T; these sequences were taken from the scanner's software libraries, and were processed with the aid of navigators using standard Siemens procedures. All the SPEN pulse sequences used in this work were custom written. In the Siemens-based experiments, these sequences were implemented while applying a suitably low G_{SPEN} gradient throughout the signal acquisition, instead of the blipped patterns illustrated in Figures 2 and 3; this was taken into account as part of the SR reconstruction by a preinterpolation of the sampled data from a zig-zagging trajectory into a Cartesian form of particular relevance was examining. For the Varian-based SPEN experiments, RF pulses and gradient shapes were designed in MATLAB® (The MathWorks, Natick, MA) and uploaded onto the scanner; in the Siemens-based experiments, RF pulses and gradient waveforms were mostly based on available Siemens software. SPEN image reconstructions were done in all instances using custom-written MATLAB packages, which included the possibility to process the SPEN-/k-space data with/without super-resolution along the spatiotemporal dimension and with weighted FT along the k-dimension. For the 2D bi-SPEN experiments, SR reconstruction was assayed both along the individual dimensions in series as well as jointly in the (x,y)-plane as described above. Pre-SR data manipulations included minor realignments of positive and negative readout echoes, zero-filling, weighting and other procedures, as described in (23). Sequences and processing codes are available upon request.

In addition to phantom tests, experiments were conducted on mice at 7T using FOVs of $30 \times 30 \times 46$ mm^3. These measurements, as well as all associated animal handling procedures, were done in accordance with protocols approved by the Weizmann Institute's Animal Care and Use Committee. A second set of in vivo experiments focused on brain imaging in human volunteers was collected on the 3T system using a 4-channels brain coil, after obtaining informed suitable written consents and following procedures approved by the Internal Review Board of the Wolfson Medical Center (Holon, Israel).

RESULTS

Phantom-Based Experiments: Quantitative Evaluations

Figure 4 compares the performance of the Hybrid sequences introduced in Figure 2, against spin-echo EPI results. These experiments were conducted on the 7T microimaging scanner using a 20 mm OD water tube possessing inside three smaller tubes, obliquely placed to better enable multislice examination. Seven 2D slices placed 1.5 mm apart were excited and scanned in single-scans, to examine the sequences' capabilities to support multislice operation. In all instances, the higher robustness of the self-refocused SPEN images vs. spin-echo EPI is clear, particularly toward the edge regions of the outer tube, affected as they are by stronger field inhomogeneity effects that get efficiently compensated by SPEN's full-refocused character. Also, evident in all EPI images are Nyquist artifacts arising from the sizable eddy currents that unavoidably arise in this narrow-bore system; despite repeated efforts for removing these effects by careful calibrations and post acquisition processing corrections, these artifacts are visible along EPI's phase-encoded dimension. These effects also show in the Hybrid SPEN images, mostly as much weaker "stripes" along the low-bandwidth (SPEN) dimension.

The relative signal- and artifact-to-noise ratios and the abilities of the various approaches to monitor adjacent slices without degrading sensitivity were also examined on this phantom. These results are summarized in Figure 5, using sums of the signal intensities observed for the various 2D images for a region limited by the walls of the outer tube. Figure 5a confirms the abilities of all sequences introduced in Figure 2 based on 180° RF pulses, to support multislicing without significant signal degradation. Most prone to saturation appear to be the Hybrid SPEN sequences introduced in Figure 2c,d; as these are based on a single swept encoding and in multiply recalled stimulated echoes, this is probably a reflection of T_1-driven losses. These effects, however, may be a price worth paying for the sake of enjoying from fully refocused single-scan images, acquired with much lower SAR values (vide infra) than those in the alternative SPEN counterparts. The sensitivity afforded by all SR SPEN sequences is also comparable to that afforded by spin-echo EPI, even upon factoring in the 50% signal loss associated with the use of stimulated echoes (Fig. 5b).

Evidence for the worthiness of seeking full-refocusing conditions is shown in Figure 6, which presents SPEN images collected with the same sequences and scanning the same phantoms as introduced in Figure 4, but with the sequences set with non-refocused $T_{180} < T_{acq}/2$ or $T_{90} < T_{acq}$ conditions. Note that, despite possessing shorter overall transverse evolution times, the latter images clearly suffer from T_2* heterogeneities which were absent under full refocusing. These are mostly evident in the regions bordering the inner and outer tube walls for slices at the edges of the z-axis FOV. Still, even in these instances, these image distortions are modest

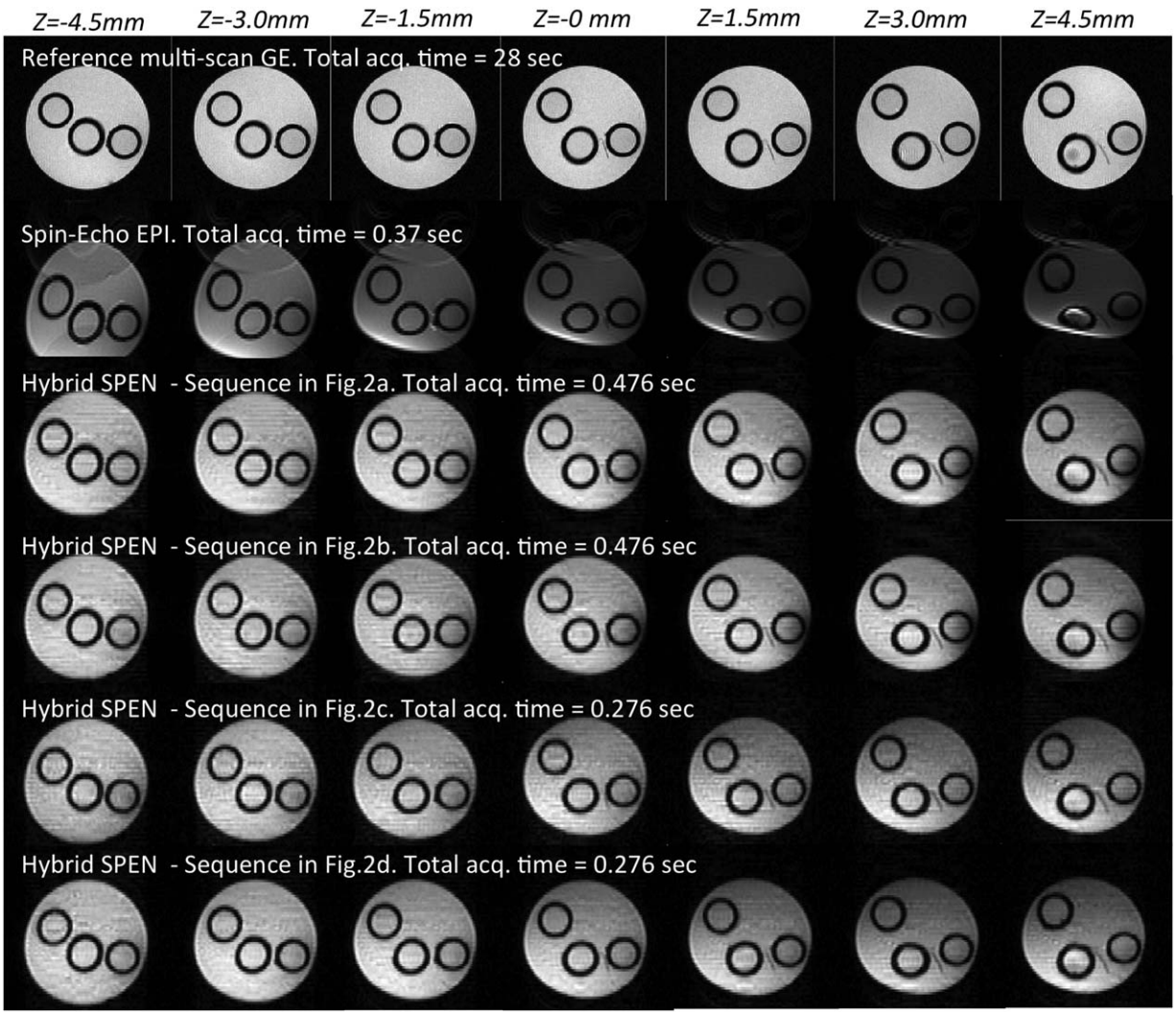

FIG. 4. Hybrid SPEN results obtained on a simple four-tube water phantom using a reference multiscan fast gradient-echo sequence, using spin-echo EPI, and with the sequences introduced in Figure 2. The total duration of each multislice acquisition is specified next to each image. Common scan parameters: FOV = 3 × 3 cm^2, resolution 0.43 × 0.43 mm^2, slice thickness 1 mm, $T_{acq} = 30.8$ ms. Hybrid SPEN with 180° chirp parameters: $T_{180} = \tau_o = 15.4$ ms, $G_{180} = 0.7$ G/cm, TE = 35 … 66 ms. Hybrid SPEN with 90° chirp parameters: $T_{90} = 30.8$ ms, $G_{90} = 0.7$ G/cm, TE = 5 … 67 ms. EPI's TE = 35 ms. Multiscan parameters: FOV = 3 × 3 cm^2, resolution 0.23 × 0.23 mm^2, slice thickness 1 mm, TE = 1.63 ms, TR = 22 ms, and $N_{averages} = 10$.

vis-à-vis those observed in SE-EPI tests under identical conditions.

Finally, it is instructive to compare these phantom-based Hybrid SPEN results, against 2D encoded bi-SPEN counterparts recorded with the sequence in Figure 3. These results are displayed in Figure 7, which compares image trains arising upon applying different reconstruction modes on the same input data set. These include a magnitude-only calculation of the kind introduced in Ref. 30), a SR procedure operating as a series of 1D reconstruction procedures acting sequentially, first along one axis and then along the other, and a full biaxial 2D SR reconstruction procedure. Although computationally more expensive than the 1D sequential procedure, taking seconds to process a 64 × 64 data matrix against milliseconds for the full sequential loop based on 1D SR processings, this biaxial 2D SR accounts for the complete spatial point-spread-function contribution of every point neighboring the encoding paraboloid, to reconstruct the spin-density at a particular r_{spc}. Interestingly, there appears to be no dramatic improvement upon adopting this complex procedure. This is probably a reflection of the relatively high definition characterizing the encoding paraboloid along the "slow" dimension in this kind of fully refocused experiments, which makes the payoff of including the "off-axis" contributions inherent to the 2D reconstruction negligible vis-à-vis processing solely the more blurred "fast" dimension. Evidence for this is also provided by: (i) comparisons against "magnitude-only" reconstructed images, which appear evidently more distorted along the "fast" than along the "slow" axes; and (ii) residual artifacts arising with either SR reconstruction method along the "fast" dimension, appearing as dark stripes along the edges of this axis and witnessing

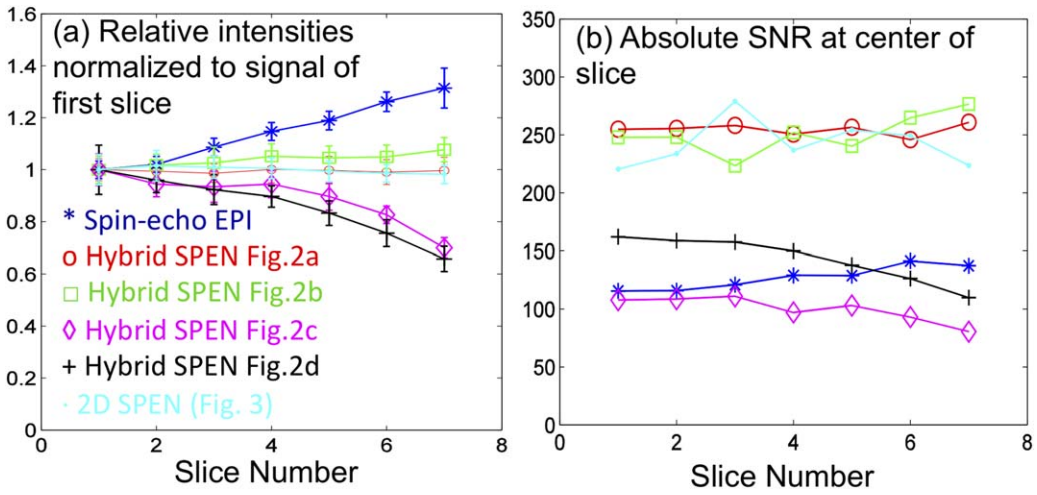

FIG. 5. Multislicing (**a**) and SNR performance (**b**) for the various SPEN sequences introduced in Figure 2, as derived from the phantom images illustrated in Figure 4. SNRs in panel (b) were estimated by averaging signals taken at the center of the phantom, and dividing these by the standard deviations measured outside the object (at the noise area). The peculiar behavior exhibited by the EPI set in (a), evidencing an apparent "increase" in signal with slice number, reflects these images' distortion due to field inhomogeneity effects, leading to a "piling up" of signal in the center of the image region used to quantify the SNR behavior (cf. second row in Fig. 4). [Color figure can be viewed in the online issue, which is available at wileyonlinelibrary.com.]

the fact that reconstruction limitations mostly arise along this dimension. In addition, worth remarking is the good multislicing performance of the sequence, leading to variations of $\leq 5\%$ among the different slices.

In addition to good sensitivity and immunity to field inhomogeneities, all the Hybrid k/SPEN sequences—and in particular the fully bi-SPEN 2D ones—have potential "zooming" abilities. This ability to focus on a particular region of interest without suffering fold-overs reflects the fact that FOV limits can be imposed by suitable design of the encoding 180° pulses: since the bandwidths of these sweeps define the encoded regions, field-of-view restrictions can be imposed by suitably choosing the range and central frequencies of corresponding chirp RF pulses, in a fashion that is reminiscent of "inner volume" EPI procedures (31). Figure 8 illustrates this in practice by comparing multiscan, multislice EPI, and multislice SPEN data, for a kumquat placed inside a well-shimmed water tube. Despite the relatively narrow water peak achieved in these 7T experiments (~60 Hz), the SPEN sequences' robustness to inhomogeneities is evident, particularly toward the contours defining the fruit edges. The frequency-selective abilities of the 2D bi-SPEN approach are illustrated in the Figure's right-most panel, which shows how the two 180° chirped pulses can be exploited for "zooming" into the inside features

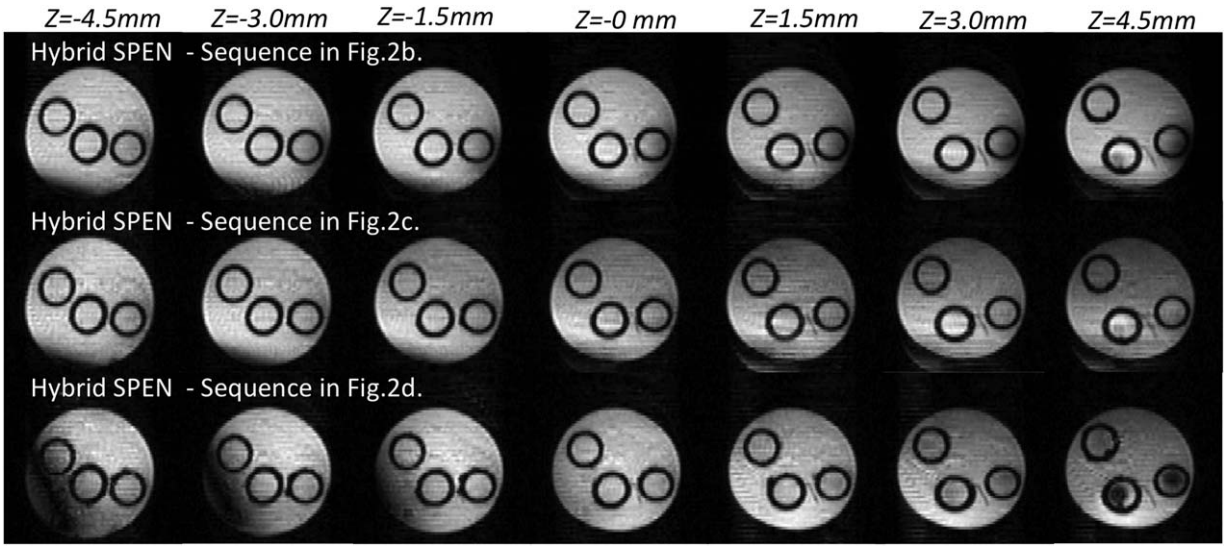

FIG. 6. Multislice Hybrid SPEN images collected for the same phantom as in Figure 4 and using many of the same sequences, but implemented away from the full-refocusing conditions. Common scan parameters: FOV = 3 × 3 cm^2, resolution 0.43 × 0.43 mm^2, slice thickness = 1 mm, and T_{acq} = 30.8 ms. Hybrid SPEN with 180° chirp parameters: T_{180} = 2 ms, τ_o = 15.4 ms, G_{180} = 5.4 G/cm, TE = 23 … 53 ms. Hybrid SPEN with 90° chirp parameters: T_{90} = 4 ms, G_{90} = 5.4 G/cm, TE = 9 … 40 ms.

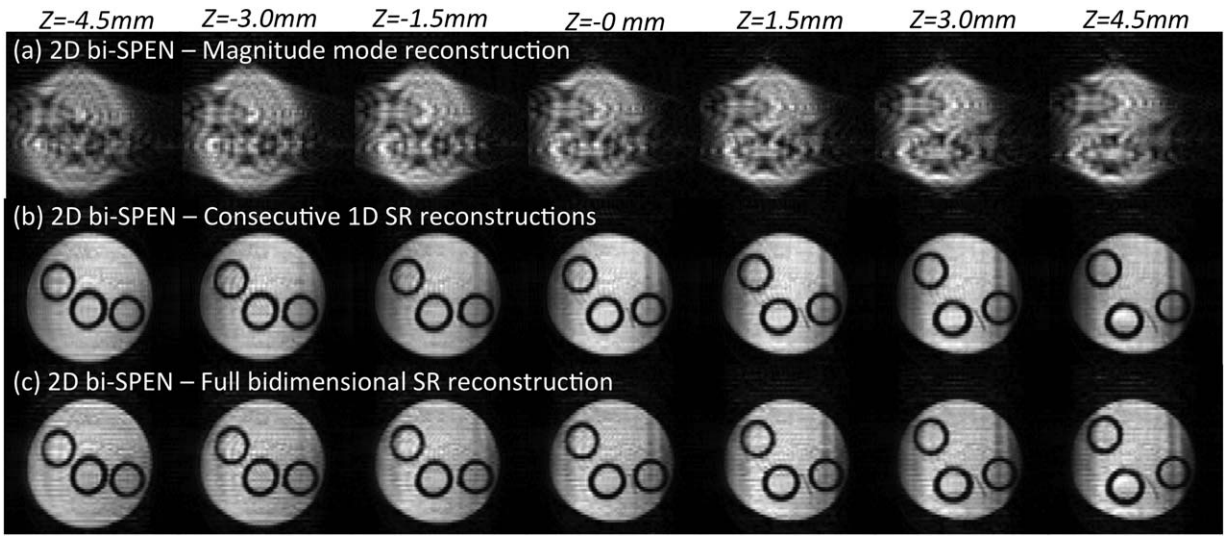

FIG. 7. Multisliced biaxial 2D SPEN images arising upon: (**a**) using a magnitude-mode reconstruction relying solely on the stationary point approximation. **b**: Applying two consecutive 1D SR loops on each of the in-plane dimensions. **c**: Using a full 2D SR reconstruction. Scan parameters: FOV = 3 × 3 cm^2, resolution 0.43 × 0.43 mm^2, slice thickness 1 mm, T_{acq}^{slow}, $T_{acq}^{fast} = 0.28\,ms$, $G_{acq}^{fast} = 21.43\,G/cm$, $T_{180}^{slow} = 15.4\,ms$, $G_{180}^{slow} = 0.7\,G/cm$, $T_{180}^{fast} = 0.8\,ms$, $G_{180}^{fast} = 3.75\,G/cm$, and TE = 36 … 67 ms.

defining the fruit's compartmentalization. By limiting in such fashion the FOV, the bi-SPEN sequence can improve the image's resolution along both the x and y directions without fold-over limitations or the need for any additional pulse/gradient manipulations.

In-Vivo Experiments

Having corroborated the sensitivity, robustness, and resolving abilities of the multisliced SPEN approaches introduced in Figures 2 and 3 on phantoms, a series of in vivo comparisons were carried out. These tests were

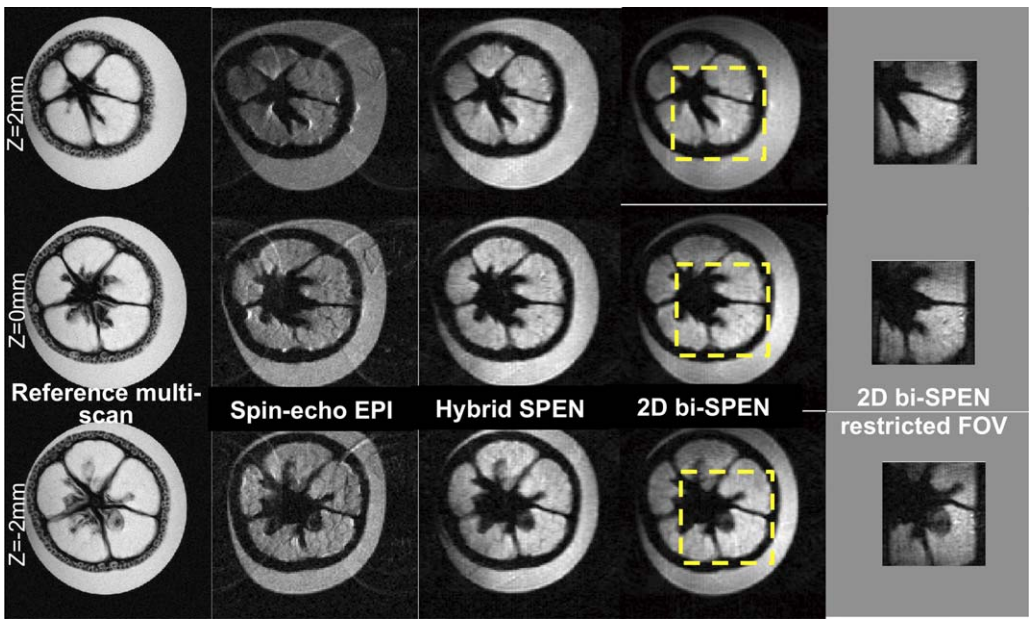

FIG. 8. Three-slice images of a kumquat collected at 7 T. From left to right: multiscan gradient echo, spin-echo EPI, Hybrid SPEN (Fig. 2b), 2D bi-SPEN, and zoomed 2D bi-SPEN results arising from the dashed yellow box. Common single shot parameters (except for the restricted-FOV data): FOV = 2.6 × 2.6 cm^2, resolution = 0.22 × 0.22 mm^2, slice thickness = 1 mm, and $T_{acq} = 48$ ms. Hybrid SPEN parameters: $T_{180} = \tau_o = 24$ ms, $G_{180} = 0.5$ G/cm. 2D bi-SPEN parameters: $T_{180}^{slow} = \tau = 24\,ms$, $G_{180}^{slow} = 0.5\,G/cm$, $T_{180}^{fast} = 0.27\,ms$, $G_{180}^{fast} = 2.5\,G/cm$, TE = 53 … 101 ms. 2D SPEN zoomed scan parameters: FOV = 1 × 1 cm^2, resolution 0.12 × 0.12 mm^2, slice thickness = 1 mm, $T_{acq} = 38.4$ ms, $T_{180}^{slow} = \tau_o = 19.2\,ms$, $G_{180}^{slow} = 1.5\,G/cm$, $T_{180}^{fast} = 0.27\,ms$, $G_{180}^{fast} = 2.67\,G/cm$, $G_{acq}^{fast} = 40\,G/cm$, TE = 43 … 81 ms. Multiscan parameters: resolution = 0.06 × 0.12 mm^2, TE = 3 ms, TR = 1 s, 2 scan averages, total scan duration = 4 min. [Color figure can be viewed in the online issue, which is available at wileyonlinelibrary.com.]

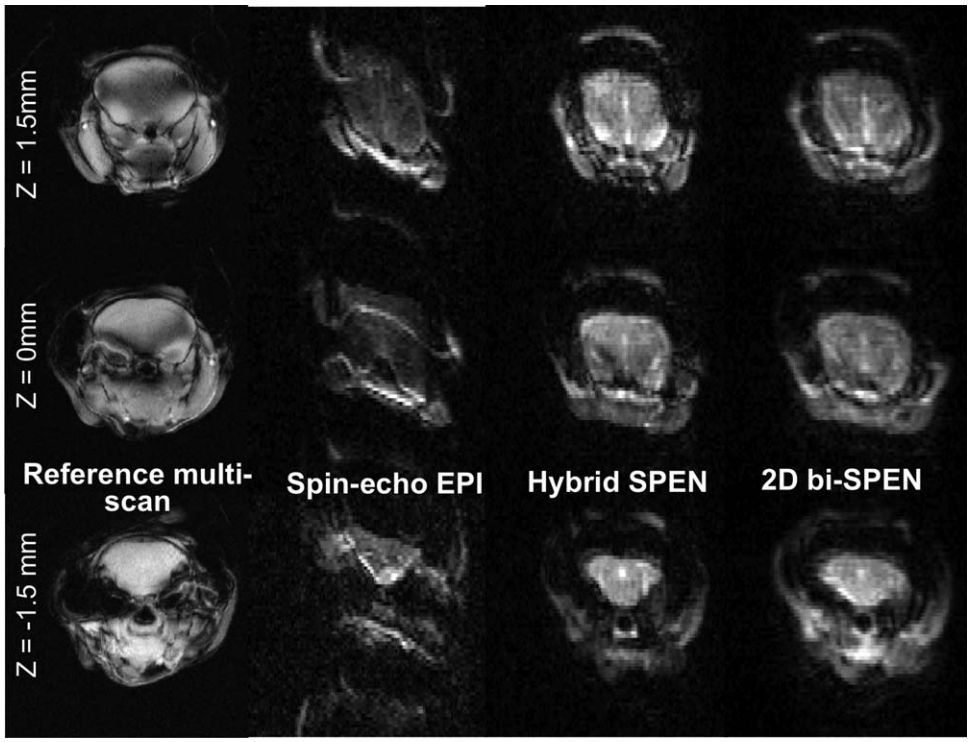

FIG. 9. Multislice in-vivo images collected at 7 T on a mouse's head, for three slices whose relative locations are indicated on the left. From left to right: Reference multiscan gradient-echo, spin-echo EPI, Hybrid SPEN (Fig. 2b) and 2D bi-SPEN images. Common single-shot parameters: FOV = 2.7 × 2.7 cm^2, resolution = 0.38 × 0.38 mm^2, slice thickness = 1.5 mm, T_{acq} = 21 ms. Hybrid SPEN parameters: $T_{180} = \tau_o = 10.5$ ms, $G_{180} = 0.7$ G/cm, TE = 26 ... 47 ms, and total scan duration 0.14 s. 2D bi-SPEN parameters: $T_{180}^{slow} = \tau_o = 10.5$ ms, $G_{180}^{slow} = 0.7\,G/cm$, $T_{180}^{fast} = 0.27$ ms, $G_{180}^{fast} = 2.12\,G/cm$, $T_{acq}^{fast} = 0.28$ ms, TE = 26 ... 47 ms, total scan duration 0.14 s. EPI parameters: TE = 21 ms, total scan duration 0.1 s. Multiscan parameters: resolution = 0.06 × 0.12 mm^2, TE = 3 ms, TR = 60 ms, 10 scan averages, and total scan duration = 2 min.

initially conducted on mice, focusing on brain imaging at 7 T and comparing once again the various SPEN-based schemes as well as EPI. Representative results arising from such experiments are show in Figure 9. As in the vertical MRI platform used for these tests the typical inhomogeneities over the full head were significant (in the presented example $\gamma\Delta B_0 = 200$ Hz), the most obvious difference among the results afforded by the various sequences reflects the much smaller distortions provided by the full-refocusing conditions. Eddy currents in this narrow-bore system also hurt the SE-EPI image reconstruction; by contrast, all these nonidealities affect SPEN to much lower extents. Also for these in vivo cases, multislice operation showed no apparent saturation effects for any of the assayed SPEN sequences.

A final set of imaging experiments is shown in Figure 10, involving 3T brain scans conducted on human volunteers. The superior field homogeneity and eddy current compensation conditions in this larger-bore scanner lead to much closer qualities between all the multislice single-scan 2D experiments assayed. Still, even in this case, the better performance of fully refocused SPEN sequences—particularly close to air/tissue interfaces—is evident. Even more noticeable advantages in the performance of the single-scan SPEN sequences are evidenced in other tissues, if these are affected by stronger heterogeneities and/or shimming limitations (data not shown). In addition, worth remarking are the different contrasts observed among the spin-echo EPI, the Hybrid 2D, and the bi-SPEN 2D images. Indeed, although in all scans the basic brain features can be identified and correlated to one another, contrast differences reflecting the effective $<T_2^*> = 0$ condition associated with full-refocusing, are evident. Also noticeable are the different T_2 weightings associated with the various encoding modes. Indeed, although all single-shot images compared in Figure 10 were acquired using minimal echo times TE (defined by the acquisition time durations), this does not mean that their T_2 weightings will be equal. In fact, for the SPEN sequences these weightings will be spatially dependent. Echo times of the fully refocused SPEN sequences based on 180° encoding pulses, for instance, start from the minimal $TE = T_{acq}$ (which would be the sole value in the SE-EPI scan) and increase thereafter (cf. Fig. 1b). The 90° chirp pulse sequence in Figure 2d by contrast, achieves full refocusing starting from an initially minimal TE = 0 echo time value. These effective TE differences reflect in the dissimilar contrasts shown by the various images in Figure 10. This includes the darker contributions of short-T_2 areas in the anterior region of the corona radiata (which were the ones endowed with the longest effective TEs for the chosen scan parameters), and the uneven T_2 weighting arising upon using the 90°-chirp

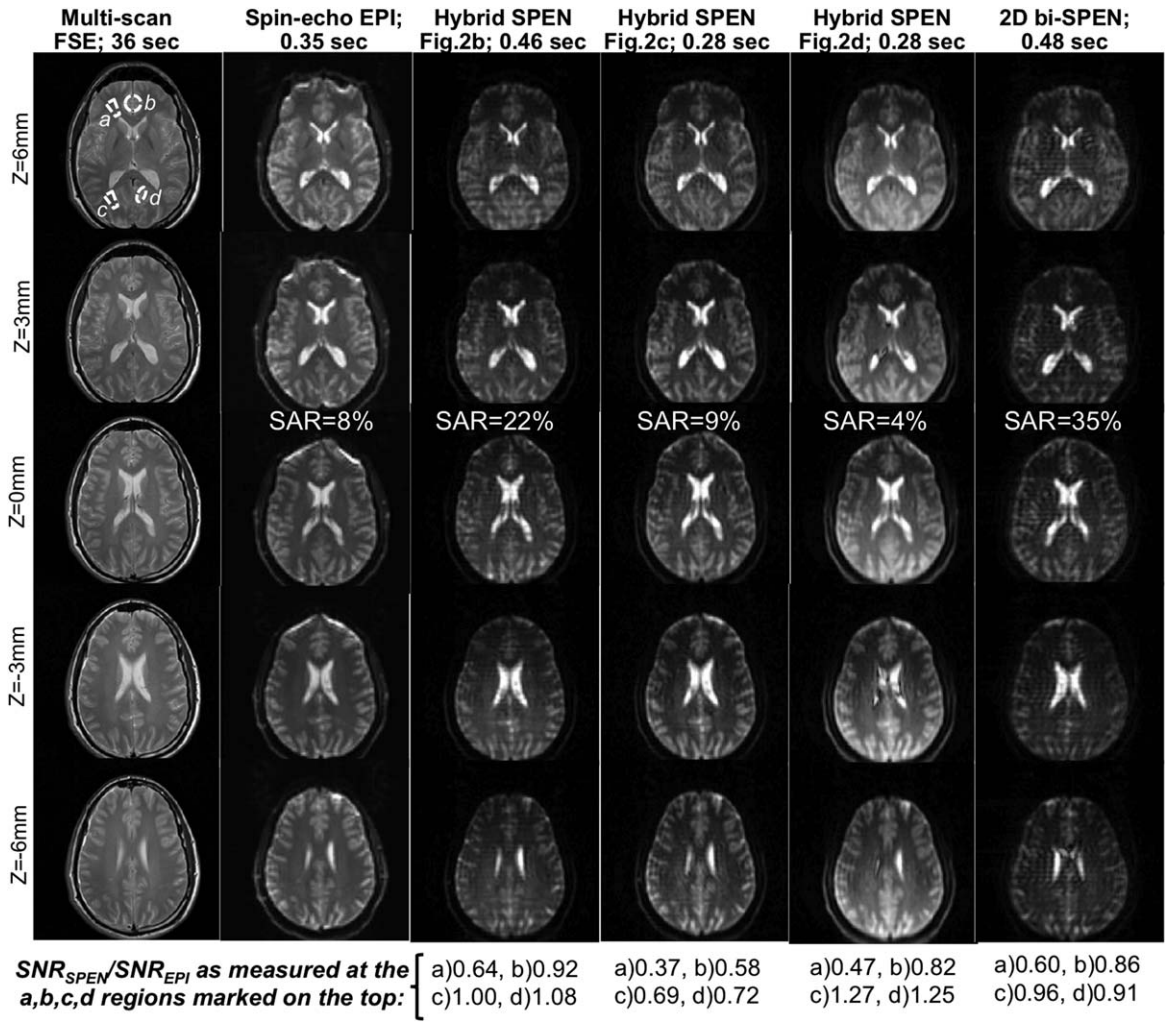

FIG. 10. Multislice images collected at 3 T on a human brain for five identical horizontal slice positions. From left to right: Reference multiscan (fast spin-echo), spin-echo EPI, Hybrid SPEN results collected with Fig. 2b–d, and 2D bi-SPEN MRI results. Common single shot sequence parameters: FOV = 22 × 22 cm^2, resolution = 2.75 × 2.75 mm^2, slice thickness = 3 mm, and T_{acq} = 42.7 ms. Hybrid parameters for the 180° adiabatic sweep sequences: $T_{180} = \tau_o = 21.3$ ms, $G_{180} = 0.04$ G/cm, and TE = 50 … 93 ms. Idem for the 90° chirp SPEN experiment: $T_{90} = 42.7$ ms, $G_{90} = 0.03$ G/cm, and TE = 7 … 93 ms. 2D bi-SPEN parameters: $T_{180}^{slow} = 21.3$ ms, $G_{180}^{slow} = 0.7$ G/cm, $T_{180}^{fast} = 1$ ms, $G_{180}^{fast} = 0.04$ G/cm, $T_{acq}^{fast} = 0.4$ ms, $G_{acq}^{fast} = 1.6$ G/cm, and TE = 53 … 96 ms. EPI's TE = 48 ms. Multiscan parameters: resolution = 0.57 × 0.57 mm^2, TE = 70 ms, TR = 1.5 s, 2 scan averaged. Also indicated for each acquisition mode are the durations for each scan (top), the SAR reported by the scanner for each acquisition (center), and the relative sensitivity vis-à-vis the spin-echo EPI experiment measured for each SPEN image, at the indicated regions (a-d, top left) for the $z = 0$ mm slices. In these latter measurements, noise was taken from signal standard deviations measured outside the object.

encoding (Fig. 2d). Still, even in these stimulated echo sequences, SNR can be on average equal or higher than in either 180°-based SPEN or SE-EPI counterparts. This is again understandable based on these sequences shorter TE's, and therefore weaker T_2 weightings. Further analyses and uses of these features are currently under progress on different organs and tissues, both in diffusion and functional studies.

DISCUSSION AND CONCLUSIONS

The experiments herein demonstrate that Hybrid k/SPEN and fully bi-SPEN 2D single shot imaging sequences can be endowed with both multislicing and full-refocusing characteristics. The resulting experiments can then serve as practical 3D imaging alternatives to EPI. If suitably timed to achieve full ΔB_o and chemical shift refocusings, all the new experiments here introduced evidence significant advantages in terms of dealing with field distortions and heterogeneities along the single-scan "slow" dimension. The sensitivity and resolution of all the new SPEN sequences is comparable to that afforded by SE EPI under optimal conditions; it can be somewhat lower if investigating short-T_2 tissues, but is usually better if dealing with field or sample inhomogeneities, thanks to the use of suitable super-resolution methods. In addition, SPEN's ability to zoom-in and thereby target small FOVs with high resolution can be desirable. A priori the SPEN modalities also include some unattractive features, foremost among these higher SARs, deriving from SPEN's use of 180° swept inversion pulses vis-à-vis the soft monochromatic RF involved in multislice EPI. As this

increase in SAR could limit short-TR applications, multislice SPEN alternatives were devised which replaced certain 180° inversion elements with stimulated echo counterparts. This decreased SAR to comparable—and in fact sometimes even lower—levels than those involved in spin-echo EPI. For example, for the experiments presented in Figure 10, the SAR percentages reported by the scanner (for multislice repetitions with TR = 3 s) were ≈8% for EPI, and only 4% when stimulated echo SPEN experiments were encoded by 90° chirps. By contrast, the use of two 180° frequency swept encoding pulses (Fig. 3a) raised 2D bi-SPEN SAR's to 35%. Despite these higher SAR values, such sequences may still prove highly useful in preclinical MRI high-field settings, both for diffusion and functional studies. Note that, while the stimulated echo sequences achieve a remarkable SAR reduction at the expense of imposing a certain degree of T_1-related weighting and signal losses onto the images, these penalties will depend on T_{acq}, on the magnetic field strength used (which in turn affects T_1s), and on the number of slices excited after each storage period. These losses can be further mitigated by letting multiple swept RF pulses target adjacent "slabs," rather than having one chirp that addresses the full SPEN dimension to be scanned. In addition, worth remarking is the fact that while all schemes hereby demonstrated display a different contrast than EPI, reflecting the varying T_1, T_2, and T_2* weightings carried by the different single-shot imaging approaches, these characteristics can be put to good use or may have to be avoided, depending on the application being sought.

The imaging experiments hereby presented highlight once again the advantages that may result from exploiting SPEN's full-refocusing features. This capability, already demonstrated in single-slice experiments based on 90° chirp pulses (24), was here extended to multislice operations based on the use of an even number of inversion pulses. This also opens the possibility of using excitation angles <90°, including potential Ernst-angle optimizations well suited to shorter recycle delays, and imaging experiments tailored to hyperpolarized systems. Further improvements worth incorporating into these volumetric experiments include the addition of parallel imaging capabilities, and "reference scan" corrections capable of accounting for the minor stripes artifacts arising upon SR reconstruction. These technical improvements, as well as practical uses of the new sequences here introduced, are currently being investigated.

ACKNOWLEDGMENTS

The authors are grateful to Amir Seginer for helpful discussions, to Dr. Nava Nevo for assistance in the animal handling procedures, and to Dr. Sagit Shushan (Wolfson Medical Center), Dr. Edna Haran and the Weizmann MRI technician team, for assistance in the human imaging scans.

REFERENCES

1. Mansfield P. Multi-planar image formation using NMR spin echoes. J Phys C: Solid State Phys 1977;10:55–58.
2. McKinnon GC. Ultrafast interleaved gradient echo planar imaging on a standard scanner. Magn Reson Med 1993;30:609–616.
3. Song AW, Wong EC, Hyde JS. Echo volume imaging. Magn Reson Med 1994;32:668–671.
4. Feinberg DA, Oshio K. GRASE (gradient and spin echo) MR imaging: a new fast clinical imaging technique. Radiology 1991;181:597–602.
5. Alsop DC. The sensitivity of low flip angle RARE imaging. Magn Reson Med 1997;37:176–184.
6. Schmitt F, Stehling MK, Turner R. Echo-planar imaging: theory, technique and application. Berlin: Springer; 1998.
7. Edelman RR, Siewert B, Darby DG, Thangaraj V, Nobre AC, Mesulam MM, Warach S. Qualitative mapping of cerebral blood flow and functional localization with echo-planar MR imaging and signal targeting with alternating radio frequency. Radiology 1994;192:513–520.
8. Turner R, Le Bihan D, Maier J, Vavrek R, Hedges LK, Pekar J. Echo-planar imaging of intravoxel incoherent motion. Radiology 1990;177:407–414.
9. Cernicanu A, Lepetit-Coiffe M, Roland J, Becker CD, Terraz S. Validation of fast MR thermometry at 1.5 T with gradient-echo echo planar imaging sequences: phantom and clinical feasibility studies. NMR Biomed 2008;21:849–858.
10. Reeder SB, Atalar E, Faranesh AZ, McVeigh ER. Referenceless interleaved echo-planar imaging. Magn Reson Med 1999;41:87–94.
11. Bernstein MA, King KF, Zhou XJ. Handbook of MRI pulse sequences. Elsevier: Academic Press; 2004.
12. Hu XP, Le TH. Artifacts reduction in EPI with phase-encoded reference scan. Magn Reson Med 1996;36:166–171.
13. Farzaneh F, Reidener SJ, Pelc NJ. Analysis of T2 limitations and off-resonance effects on spatial resolution and artifacts in echo-planar imaging. Magn Reson Med 1990;14:123–139.
14. Xu D, King KF, Zur Y, Hinks RS. Robust 2D phase correction for echo planar imaging under a tight field-of-view. Magn Reson Med 2010;64:1800–1813.
15. Kunz D. Use of frequency-modulated radiofrequency pulses in MR imaging experiments. Magn Reson Med 1986;3:377–384.
16. Pipe JG. Spatial encoding and reconstruction in MRI with quadratic phase profiles. Magn Reson Med 1995;33:24–33.
17. Frydman L, Scherf T, Lupulescu A. The acquisition of multidimensional nmr spectra within a single scan. Proc Natl Acad Sci 2002;99:15858.
18. Tal A, Frydman L. Single-scan multidimensional magnetic resonance. Prog Nucl Magn Reson Spectrosc 2010;57:241–292.
19. Shrot Y, Frydman L. Spatially-encoded NMR and the acquisition of 2D magnetic resonance images within a single scan. J Magn Reson 2005;172:179–190.
20. Chamberlain R, Park JY, Corum C, Yacoub E, Ugurbil K, Jack CR Jr., Garwood M. RASER: a new ultrafast magnetic resonance imaging method. Magn Reson Med 2007;58:794–799.
21. Chen Y, Li J, Qu X, Chen L, Cai C, Cai S, Zhong J, Chen Z. Partial Fourier transform reconstruction for single-shot MRI with linear frequency-swept excitation. Magn Reson Med 2013;69:1326–1336.
22. Shen J, Xiang Y. High fidelity magnetic resonance imaging by frequency sweep encoding and Fourier decoding. J Magn Reson 2010;204:200–207.
23. Ben-Eliezer N, Irani M, Frydman L. Super-resolved spatially-encoded single-scan 2D MRI. Magn Reson Med 2010;63:1594–1600.
24. Ben-Eliezer N, Shrot Y, Frydman L. High-definition single-scan 2D MRI in inhomogeneous fields using spatial encoding methods. Magn Reson Imag 2010;28:77–86.
25. Goerke U, Garwood M, Ugurbil K. Functional magnetic resonance imaging using RASER. Neuroimage 2011;54:350–360.
26. Ben-Eliezer N, Goerke U, Ugurbil K, Frydman L. Functional MRI using super-resolved spatiotemporally-encoded imaging techniques. Magn Reson Imaging 2012;30:1401–1408.
27. Tal A, Frydman L. Spectroscopic imaging from spatially-encoded single-scan multidimensional MRI data. J Magn Reson 2007;189:46–58.
28. Schmidt R, Frydman L. In vivo 3D spatial/1D spectral imaging by spatiotemporal encoding: a new single-shot experimental and processing approach. Magn Reson Med 2013;70:382–391.
29. Ben-Eliezer N, Frydman L. Spatiotemporal encoding as a robust basis for fast three-dimensional in vivo MRI. NMR Biomed 2011;24:1191–1201.
30. Tal A, Frydman L. Spatial encoding and the acquisition of high definition MR images in inhomogeneous magnetic fields. J Magn Reson 2006;181:179–194.
31. Feinberg DA, Hoenninger JC, Crooks LE, Kaufman L, Watts JC, Arakawa M. Inner volume MR imaging: technical concepts and their application. Radiology 1985;156:743–747.